1-1-2008

First measurement of target and double spin asymmetries for e [over→] p [over→]→ epπ^{0} in the nucleon resonance region above the Δ (1232)

Angela Biselli
Fairfield University, abiselli@fairfield.edu

CLAS Collaboration

Peer Reviewed

Repository Citation

Biselli, Angela and CLAS Collaboration, "First measurement of target and double spin asymmetries for e [over→] p [over→]→ epπ^{0} in the nucleon resonance region above the Δ (1232)" (2008). *Physics Faculty Publications*. 17.
http://digitalcommons.fairfield.edu/physics-facultypubs/17

Published Citation

Biselli, A. S., et al. [CLAS Collaboration] "First measurement of target and double spin asymmetries for e [over→] p [over→]→ epπ^{0} in the nucleon resonance region above the Δ (1232)." Physical Review C 78.4 (2008): 045204. DOI: 10.1103/PhysRevC.78.045204

First measurement of target and double spin asymmetries for $\vec{e}\,\vec{p} \to ep\pi^0$ in the nucleon resonance region above the $\Delta(1232)$

A. S. Biselli,[11,*] V. D. Burkert,[34] M. J. Amaryan,[29] G. Asryan,[39] H. Avakian,[34] H. Bagdasaryan,[29] N. Baillie,[38] J. P. Ball,[2] N. A. Baltzell,[33] M. Battaglieri,[19] I. Bedlinskiy,[21] M. Bellis,[5] N. Benmouna,[15] B. L. Berman,[15] L. Blaszczyk,[14] C. Bookwalter,[14] S. Boiarinov,[34] P. Bosted,[34] R. Bradford,[5] D. Branford,[10] W. J. Briscoe,[15] W. K. Brooks,[12] S. Bültmann,[29] C. Butuceanu,[38] J. R. Calarco,[26] S. L. Careccia,[29] D. S. Carman,[34] L. Casey,[6] S. Chen,[14] L. Cheng,[6] P. L. Cole,[17] P. Collins,[2] P. Coltharp,[14] D. Crabb,[37] V. Crede,[14] D. Dale,[17] N. Dashyan,[39] R. De Masi,[7] R. De Vita,[19] E. De Sanctis,[18] P. V. Degtyarenko,[34] A. Deur,[34] S. Dhamija,[13] R. Dickson,[5] C. Djalali,[33] G. E. Dodge,[29] D. Doughty,[8,34] M. Dugger,[2] O. P. Dzyubak,[33] H. Egiyan,[34,†] L. El Fassi,[1] L. Elouadrhiri,[34] P. Eugenio,[14] G. Fedotov,[25] R. Feuerbach,[5] R. Fersch,[38] T. A. Forest,[17] A. Fradi,[20] M. Garçon,[7] G. Gavalian,[29,†] N. Gevorgyan,[39] G. P. Gilfoyle,[32] K. L. Giovanetti,[22] F. X. Girod,[7] J. T. Goetz,[3] W. Gohn,[9] R. W. Gothe,[33] L. Graham,[33] K. A. Griffioen,[38] M. Guidal,[20] N. Guler,[29] L. Guo,[34] V. Gyurjyan,[34] K. Hafidi,[1] H. Hakobyan,[39] C. Hanretty,[14] N. Hassall,[16] K. Hicks,[28] I. Hleiqawi,[28] M. Holtrop,[26] C. E. Hyde-Wright,[29] Y. Ilieva,[15,‡] D. G. Ireland,[16] B. S. Ishkhanov,[25] E. L. Isupov,[25] M. M. Ito,[34] D. Jenkins,[36] H. S. Jo,[20] J. R. Johnstone,[16] K. Joo,[9] H. G. Juengst,[29] N. Kalantarians,[29] D. Keller,[28] J. D. Kellie,[16] M. Khandaker,[27] W. Kim,[23] A. Klein,[29] F. J. Klein,[6] M. Kossov,[21] Z. Krahn,[5] V. Kubarovsky,[34] J. Kuhn,[5] S. E. Kuhn,[29] S. V. Kuleshov,[21] V. Kuznetsov,[23] J. Lachniet,[29] J. M. Laget,[34,§] J. Langheinrich,[33] D. Lawrence,[24] K. Livingston,[16] H. Y. Lu,[33] M. MacCormick,[20] N. Markov,[9] P. Mattione,[31] B. McKinnon,[16] J. W. C. McNabb,[5] B. A. Mecking,[34] M. D. Mestayer,[34] C. A. Meyer,[5] T. Mibe,[28] K. Mikhailov,[21] M. Mirazita,[18] V. Mokeev,[25,34] B. Moreno,[20] K. Moriya,[5] S. A. Morrow,[7,20] M. Moteabbed,[13] E. Munevar,[15] G. S. Mutchler,[31] P. Nadel-Turonski,[15] R. Nasseripour,[33,‖] S. Niccolai,[20] G. Niculescu,[22] I. Niculescu,[22] B. B. Niczyporuk,[34] M. R. Niroula,[29] R. A. Niyazov,[30] M. Nozar,[34] M. Osipenko,[19,25] A. I. Ostrovidov,[14] K. Park,[33] S. Park,[14] E. Pasyuk,[2] C. Paterson,[16] S. Anefalos Pereira,[18] J. Pierce,[37] N. Pivnyuk,[21] O. Pogorelko,[21] S. Pozdniakov,[21] J. W. Price,[4] Y. Prok,[37,¶] D. Protopopescu,[16] B. A. Raue,[13,34] G. Ricco,[19] M. Ripani,[19] B. G. Ritchie,[2] G. Rosner,[16] P. Rossi,[18] F. Sabatié,[7] M. S. Saini,[14] J. Salamanca,[17] C. Salgado,[27] J. P. Santoro,[6] V. Sapunenko,[34] D. Schott,[13] R. A. Schumacher,[5] V. S. Serov,[21] Y. G. Sharabian,[34] D. Sharov,[25] N. V. Shvedunov,[25] E. S. Smith,[34] D. I. Sober,[6] D. Sokhan,[10] A. Stavinsky,[21] S. S. Stepanyan,[23] S. Stepanyan,[34] B. E. Stokes,[14] P. Stoler,[30] I. I. Strakovsky,[15] S. Strauch,[33] M. Taiuti,[19] D. J. Tedeschi,[33] A. Tkabladze,[15,**] S. Tkachenko,[29] L. Todor,[5] M. Ungaro,[9] M. F. Vineyard,[35] A. V. Vlassov,[21] D. P. Watts,[16,††] L. B. Weinstein,[29] D. P. Weygand,[34] M. Williams,[5] E. Wolin,[34] M. H. Wood,[33,‡‡] A. Yegneswaran,[34] M. Yurov,[23] L. Zana,[26] J. Zhang,[29] B. Zhao,[9] and Z. W. Zhao[33]

[1]*Argonne National Laboratory, Argonne, Illinois 60439, USA*
[2]*Arizona State University, Tempe, Arizona 85287-1504, USA*
[3]*University of California, Los Angeles, California 90095-1547, USA*
[4]*California State University, Dominguez Hills, Carson, California 90747, USA*
[5]*Carnegie Mellon University, Pittsburgh, Pennsylvania 15213, USA*
[6]*Catholic University of America, Washington, D.C. 20064, USA*
[7]*CEA-Saclay, Service de Physique Nucléaire, F-91191 Gif-sur-Yvette, France*
[8]*Christopher Newport University, Newport News, Virginia 23606, USA*
[9]*University of Connecticut, Storrs, Connecticut 06269, USA*
[10]*Edinburgh University, Edinburgh EH9 3JZ, United Kingdom*
[11]*Fairfield University, Fairfield, Connecticut 06824, USA*
[12]*Universidad Técnica Federico Santa María, Casilla 110-V, Valparaíso, Chile*
[13]*Florida International University, Miami, Florida 33199, USA*
[14]*Florida State University, Tallahassee, Florida 32306, USA*
[15]*The George Washington University, Washington, D.C. 20052, USA*
[16]*University of Glasgow, Glasgow G12 8QQ, United Kingdom*
[17]*Idaho State University, Pocatello, Idaho 83209, USA*
[18]*INFN, Laboratori Nazionali di Frascati, I-00044 Frascati, Italy*
[19]*INFN, Sezione di Genova, I-16146 Genova, Italy*
[20]*Institut de Physique Nucleaire ORSAY, Orsay, France*
[21]*Institute of Theoretical and Experimental Physics, Moscow RU-117259, Russia*
[22]*James Madison University, Harrisonburg, Virginia 22807, USA*
[23]*Kyungpook National University, Daegu 702-701, Republic of Korea*
[24]*University of Massachusetts, Amherst, Massachusetts 01003, USA*
[25]*Moscow State University, General Nuclear Physics Institute, Moscow RU-119899, Russia*
[26]*University of New Hampshire, Durham, New Hampshire 03824-3568, USA*
[27]*Norfolk State University, Norfolk, Virginia 23504, USA*
[28]*Ohio University, Athens, Ohio 45701, USA*
[29]*Old Dominion University, Norfolk, Virginia 23529, USA*
[30]*Rensselaer Polytechnic Institute, Troy, New York 12180-3590, USA*

^{31}*Rice University, Houston, Texas 77005-1892, USA*

^{32}*University of Richmond, Richmond, Virginia 23173, USA*

^{33}*University of South Carolina, Columbia, South Carolina 29208, USA*

^{34}*Thomas Jefferson National Accelerator Facility, Newport News, Virginia 23606, USA*

^{35}*Union College, Schenectady, New York 12308, USA*

^{36}*Virginia Polytechnic Institute and State University, Blacksburg, Virginia 24061-0435, USA*

^{37}*University of Virginia, Charlottesville, Virginia 22901, USA*

^{38}*College of William and Mary, Williamsburg, Virginia 23187-8795, USA*

^{39}*Yerevan Physics Institute, 375036 Yerevan, Armenia*

The exclusive channel $\vec{p}(\vec{e}, e'p)\pi^0$ was studied in the first and second nucleon resonance regions in the Q^2 range from 0.187 to 0.770 GeV^2 at Jefferson Lab using the CEBAF Large Acceptance Spectrometer. Longitudinal target and beam-target asymmetries were extracted over a large range of center-of-mass angles of the π^0 and compared to the unitary isobar model MAID, the dynamic model by Sato and Lee, and the dynamic model DMT. A strong sensitivity to individual models was observed, in particular for the target asymmetry and in the higher invariant mass region. This data set, once included in the global fits of the above models, is expected to place strong constraints on the electrocoupling amplitudes $A_{1/2}$ and $S_{1/2}$ for the Roper resonance $N(1400)P_{11}$ and the $N(1535)S_{11}$ and $N(1520)D_{13}$ states.

I. INTRODUCTION

Studying the structure of the nucleon and its excitations is essential in the development of an understanding of the strong interaction at the confinement scale [1]. On a fundamental level there exists only a limited understanding of the relationship between quantum chromodynamics (QCD), the field theory of the strong interaction, and models that use effective degrees of freedom, such as the large variety of constituent quark models or alternative hadron models [2–6]. Experimentally, we still lack sufficiently complete data sets that can be used in phenomenological analyses to unravel the internal structure of the nucleon's excited states by determining their electromagnetic transition amplitudes for different distance scales. Precise cross-section and polarization data for π^0 production off protons, which are needed to study the transition from the nucleon ground state to the $\Delta(1232)$, have become available in recent years. For a recent review see Ref. [7]. These data have been used to extract the electromagnetic

transition multipoles for this state over a wide range of photon virtuality Q^2 [8–16]. These accurate data have been confronted with recent results from quenched lattice QCD calculations [17,18].

The $\Delta(1232)P_{33}$ excitation corresponds to the transition between isospin 1/2 and isospin 3/2 ground states of the nonstrange baryons and is characterized by a spin flip in the ground state. To study the radial and orbital excitations of the nucleon, we need to measure the transition form factors for higher-mass states. In the mass region above the $\Delta(1232)P_{33}$, there is a cluster of resonances around 1.5 GeV that consists of three isospin 1/2 nucleon excitations. The $N(1440)P_{11}$, often called the Roper resonance, is thought of as the first radial excitation of the nucleon. The two other states, the $N(1520)D_{13}$ and $N(1535)S_{11}$, are orbital excitations of the nucleon. By measuring the transition form factors of these states, we probe the radial and orbital wave function of the nucleon that describe fundamental properties of the nucleon structure at the constituent quark and meson-nucleon scales. In the mass range around 1.7 GeV, there is a cluster of nine resonances that consists of a number of isospin 1/2 and isospin 3/2 states in various configurations of radial and orbital excitations of the three-quark system. These resonances overlap with each other and contain higher-partial waves. This mass range is also characterized by significant nonresonant contributions to the production cross section. To separate these states, and isolate them from nonresonant contributions, more experimental information is required than in the case of the $\Delta(1232)$. Measurements of different isospin channels, e.g., $p\pi^0$ and $n\pi^+$ final states, are essential. Measurements with polarized beam and polarized target, and measurements of the proton recoil polarization, are highly sensitive to interferences of resonant and nonresonant amplitudes contributing to pion production. These data are indispensable for isolating individual resonances and determining their excitation strengths within the framework of any model.

---

*biselli@jlab.org

†Current address: University of New Hampshire, Durham, New Hampshire 03824-3568, USA.

‡Current address: University of South Carolina, Columbia, South Carolina 29208, USA.

§Current address: CEA-Saclay, Service de Physique Nucléaire, 91191 Gif-sur-Yvette, France.

$^\parallel$Current address: The George Washington University, Washington, D.C., 20052, USA.

¶Current address: Massachusetts Institute of Technology, Cambridge, Massachusetts 02139-4307, USA.

**Current address: Ohio University, Athens, Ohio 45701, USA.

††Current address: Edinburgh University, Edinburgh EH9 3JZ, United Kingdom.

‡‡Current address: University of Massachusetts, Amherst, Massachusetts 01003, USA.

The mass range above the $\Delta(1232)$ has recently been systematically mapped out in measurements of unpolarized cross sections of the electroproduction processes $ep \to en\pi^+$ [19, 20], $ep \to ep\pi^0$ [9], $ep \to ep\eta$ [21–23], and $ep \to ep\pi^+\pi^-$ [24,25], and measurements of beam spin asymmetries using polarized electron beams [19,26]. Detailed measurements with polarized beams and polarized targets were carried out in inclusive electron scattering in the resonance region [27–29], and a limited number of data points were measured for the $\vec{e}\vec{p} \to en\pi^+$ reaction with polarized proton targets [30]. However, no data are available for the processes $e\vec{p} \to ep\pi^0$ and $\vec{e}\vec{p} \to ep\pi^0$. The intent of the current research has been to fill this gap and to provide precise and detailed data from measurements for the $p\pi^0$ final state using both polarized electrons and a polarized proton target, and to systematically map the mass region from $W = 1.1$ GeV to $W = 1.7$ GeV and in the range $0.187 < Q^2 < 0.770 \, \mathrm{GeV}^2$.

II. FORMALISM

The $\vec{e}\vec{p} \to ep\pi^0$ reaction is schematically shown in Fig. 1. The incident polarized electron is given by the four-vector $p_e = (\vec{p}_e, E_i)$, the outgoing electron is emitted with angles ϕ_e, θ_e and four-vector $p'_e = (\vec{p}'_e, E_f)$, and the nucleon initial and final states are given by $p_p = (0, M)$ and $p'_p = (\vec{p}'_p, E_p)$, respectively. The virtual photon γ^* with four-vector $q = (\vec{q}, \omega)$, where $\vec{q} = \vec{p}_e - \vec{p}'_e$ and $\omega = E_i - E_f$ is characterized by the squared four-momentum transfer:

$$Q^2 = -q^2 = -(\omega^2 - |\vec{q}|^2) = 4E_f E_i \sin^2 \frac{\theta_e}{2} \qquad (1)$$

and the degree of transverse polarization:

$$\epsilon = \left(1 + 2\frac{|\vec{q}|^2}{Q^2} \tan^2 \frac{\theta_e}{2}\right)^{-1}. \qquad (2)$$

The invariant mass of the hadronic system is given by:

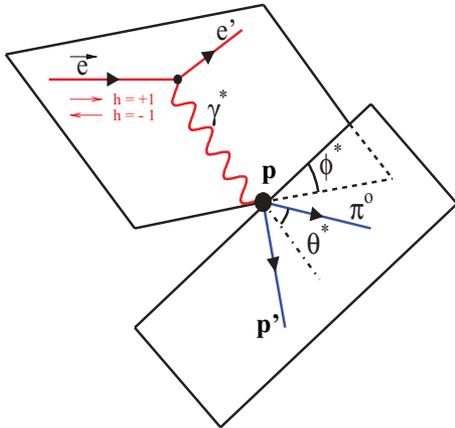$$W = |p_e + p_p - p'_e| = \sqrt{M^2 + 2M\omega - Q^2}. \qquad (3)$$

FIG. 1. (Color online) Schematic diagram of π^0-nucleon electroproduction. $\vec{e}$ represents the incident polarized electron, e' is the outgoing electron, γ^* is the virtual photon, and p and p' are the nucleon in the initial and final states, respectively.

In terms of these variables the differential cross section can be written as:

$$\frac{d^5\sigma}{dE_f d\Omega_e d\Omega^*} = \Gamma \frac{d\sigma}{d\Omega^*}, \qquad (4)$$

where $d\Omega_e = \sin\theta_e d\theta_e d\phi_e$ is the electron solid angle and $d\Omega^* = \sin\theta^* d\theta^* d\phi^*$ is the solid angle of the meson in the center-of-mass (c.m.). Here

$$\Gamma = \frac{\alpha}{2\pi^2} \frac{E_f}{E_i} \frac{k_\gamma^{\mathrm{lab}}}{Q^2} \frac{1}{1-\epsilon} \qquad (5)$$

is the virtual photon flux, where

$$k_\gamma^{\mathrm{lab}} = \frac{W^2 - M^2}{2M} \qquad (6)$$

denotes the "photon equivalent energy" necessary for a real photon to excite a hadronic system with center-of-mass energy W, and α is the fine structure constant.

The differential cross section for pion production by a virtual photon $d\sigma/d\Omega^*$ can be written as a sum of four terms:

$$\frac{d\sigma}{d\Omega^*} = \frac{|\vec{k}|}{k_\gamma^{\mathrm{c.m.}}} \left(\frac{d\sigma_0}{d\Omega^*} + h\frac{d\sigma_e}{d\Omega^*} + P\frac{d\sigma_t}{d\Omega^*} + hP\frac{d\sigma_{\mathrm{et}}}{d\Omega^*} \right), \quad (7)$$

where $\vec{k}$ is the momentum of the pion, h is the electron helicity, and P is the target proton polarization. The first term $d\sigma_0/d\Omega^*$ represents the unpolarized cross section, whereas the remaining terms $d\sigma_e/d\Omega^*$, $d\sigma_t/d\Omega^*$, and $d\sigma_{\mathrm{et}}/d\Omega^*$ arise when beam, target, or both beam and target are polarized, respectively. Here

$$k_\gamma^{\mathrm{c.m.}} = \frac{M}{W} k_\gamma^{\mathrm{lab}} \qquad (8)$$

is the "real photon equivalent energy" in the center-of-mass frame. These cross sections can be written in terms of response functions R using the formalism of reference [31] as:

$$\frac{d\sigma_0}{d\Omega^*} = R_T^0 + \epsilon_L R_L^0 + \sqrt{2\epsilon_L(1+\epsilon)}R_{TL}^0 \cos\phi^*$$
$$+ \epsilon R_{TT}^0 \cos 2\phi^*$$

$$\frac{d\sigma_e}{d\Omega^*} = \sqrt{2\epsilon_L(1-\epsilon)}R_{TL'}^0 \sin\phi^*$$

$$\frac{d\sigma_t}{d\Omega^*} = \sin\theta_\gamma \cos\phi^* \left[\sqrt{2\epsilon_L(1+\epsilon)}R_{TL}^x \sin\phi^* \right.$$
$$+ \epsilon R_{TT}^x \sin 2\phi^* \Big] + \sin\theta_\gamma \sin\phi^* \Big[R_{TL}^y + \epsilon_L R_L^y$$
$$+ \sqrt{2\epsilon_L(1+\epsilon)}R_{TL}^y \cos\phi^* + \epsilon R_{TT}^y \cos 2\phi^* \Big]$$
$$+ \cos\theta_\gamma \left[\sqrt{2\epsilon_L(1+\epsilon)}R_{TL}^z \sin\phi^* + \epsilon R_{TT}^z \sin 2\phi^* \right]$$

$$\frac{d\sigma_{\mathrm{et}}}{d\Omega^*} = -\sin\theta_\gamma \left[\sqrt{2\epsilon_L(1-\epsilon)}R_{TL'}^x \cos\phi^{*2} \right.$$
$$+ \sqrt{1-\epsilon^2}R_{TT'}^x \cos\phi^* \Big]$$
$$+ \sin\theta_\gamma \sqrt{2\epsilon_L(1-\epsilon)}R_{TL'}^y \sin\phi^{*2}$$
$$- \cos\theta_\gamma \left[\sqrt{2\epsilon_L(1-\epsilon)}R_{TL'}^z \cos\phi^* + \sqrt{1-\epsilon^2}R_{TT'}^z \right],$$
$$(9)$$

where

$$\epsilon_L = \frac{Q^2}{\omega^2}\epsilon \qquad (10)$$

is the frame-dependent longitudinal polarization of the virtual photon. The θ_γ is the angle between the directions of the target polarization and the virtual photon.

The asymmetries are then defined as:

$$A_e = \frac{\sigma_e}{\sigma_0}$$
$$A_t = \frac{\sigma_t}{\sigma_0} \qquad (11)$$
$$A_{et} = -\frac{\sigma_{et}}{\sigma_0},$$

where $\sigma_0 \equiv d\sigma_0/d\Omega^*$, $\sigma_e \equiv d\sigma_e/d\Omega^*$, $\sigma_t \equiv d\sigma_t/d\Omega^*$, and $\sigma_{et} \equiv d\sigma_{et}/d\Omega^*$.

If integrated over the azimuthal center-of-mass angle ϕ^*, the double spin asymmetry A_{et} can be parameterized as [32]:

$$A_{et} = \sqrt{1-\epsilon^2}\cos\theta_\gamma \frac{A_1 + \eta A_2}{1 + \epsilon R}, \qquad (12)$$

where $\eta = \tan\theta_\gamma\sqrt{2\epsilon/(1+\epsilon)}$ and R is the longitudinal-transverse cross section ratio σ_L/σ_T The structure function A_1 is the virtual photon helicity asymmetry,

$$A_1 = \frac{|A_{1/2}|^2 - |A_{3/2}|^2}{|A_{1/2}|^2 + |A_{3/2}|^2}, \qquad (13)$$

whereas A_2 is a longitudinal-transverse interference term.

III. REACTION MODELS

In recent years, several models have been developed that aim at accurately reproducing the experimental data. In Sec. VI we compare some of our data with calculations based on model descriptions such as the Dubna-Mainz-Taipei (DMT) model [2], a recent version of the MAID model [3], and the Sato-Lee model (SL) [4]. In addition, a unitary isobar model (UIM) was developed by the Yerevan-JLab group [5,6] that contains many features of MAID but incorporates different energy dependences of the background amplitudes at higher energies. This approach allows the fitting of experimental cross sections and polarization asymmetries and the extraction of resonance transition amplitudes from a large body of data. We briefly summarize the main features of these models. They are discussed in more detail in Ref. [7].

MAID and related models are based on an isobar description of the single pion production process. They incorporate nonresonant amplitudes described by tree-level Born terms and also include ρ- and ωt-channel processes that are relevant mostly in the region of higher resonances. Figure 2 shows the diagrams contributing to the reaction $ep \to ep\pi^0$ at low and intermediate energies. The vertex functions for the virtual photon coupling to hadrons are parameterized according to their respective on-shell form factors for which there is prior experimental information. Resonances are parameterized by a phenomenological description using a relativistic Breit-Wigner form with an energy-dependent width. The total am-
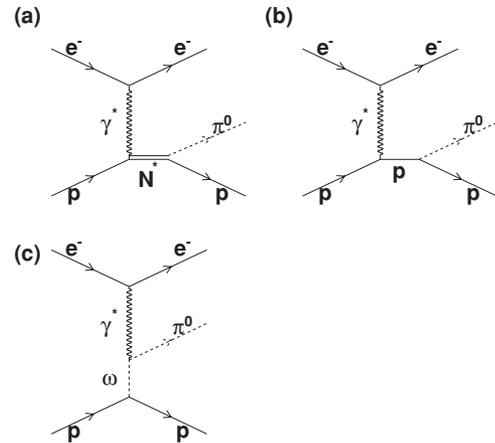

FIG. 2. Tree-level diagrams of single $p\pi^0$ electroproduction for (a) *s*-channel resonance production, (b) *s*-channel nucleon exchange, and (c) *t*-channel ω meson exchange.

plitude for single pion production is unitarized in a *K*-matrix formulation. Only single channels are included, and multichannel effects such as $\gamma N \to (\rho N, \pi\Delta) \to \pi N$, which could be important in the second and third resonance regions, are neglected. From an experimental viewpoint, the attractive feature of these descriptions is flexibility that allows adjusting parameters such as electromagnetic transition form factors and hadronic couplings as new experimental information becomes available. However, all of these descriptions lack significant predictive power, and a comparison with new data will tell us more about how well electromagnetic and hadronic couplings have been parameterized rather than about the intrinsic structure of the nucleon.

Dynamical models, such as the SL and DMT models start from a consistent Hamiltonian formulation. In these models, the nonresonant interaction modifies the resonant amplitude. The SL model provides the most consistent description of the interaction but is currently limited to the region of the $\Delta(1232)$ resonance, whereas in the DMT model the resonance amplitudes are parameterized according to a specific Breit-Wigner form that simplifies the inclusion of higher resonances. The *s*-channel resonance parametrization in the DMT model is similar to what is used in the isobar descriptions such as the MAID and UIM approaches. Once the transition form factors have been extracted from the data, their interpretation in terms of the intrinsic structure of the nucleon must then involve comparisons with nucleon structure models, such as the many versions of the constituent quark model's (CQM) and lattice QCD calculations.

IV. EXPERIMENTAL SETUP

Measurements were performed in 2000–2001 using the CEBAF Large Acceptance Spectrometer (CLAS) [33] at the Thomas Jefferson National Accelerator Facility (Jefferson Lab), located in Newport News, Virginia. The experiment consisted of a longitudinally polarized electron beam with energies from 1.6 to 5.6 GeV and currents ranging from 1 to 5 nA, scattering off longitudinally polarized protons and

deuterons in ammonia targets, $^{15}NH_3$ and $^{15}ND_3$. The beam was rastered in a spiral pattern of 1–1.2 cm diameter over the target to avoid destroying the target polarization due to beam heating. The beam had an average polarization of 70%, and the polarization direction was reversed with a frequency of 30 Hz.

The experiment used two frozen ammonia targets, $^{15}NH_3$ and $^{15}ND_3$, and ^{12}C, ^{4}He, and ^{15}N targets for background studies. The targets were held in a 1 K liquid-helium cooling bath and a 5 T longitudinal magnetic field generated by a pair of superconducting Helmholtz coils, which blocked particles scattered at polar angles between $45°$ and $70°$. The protons and deuterons in the ammonia were polarized via dynamic nuclear polarization and the polarization achieved was about 75% for protons and 25% deuterons.

The scattered particles were detected using the CLAS detector, described in great detail in Ref. [33]. The CLAS detector consists of six superconducting coils that produce a toroidal field, around the beam direction, which bends charged particles in the polar direction but leaves them nearly unaffected in the azimuthal direction. The polarity of the magnetic field was set to bend negative particles toward the beam line. Each of six sectors, delimited by the coils, are equipped with three drift chamber (DC) regions to determine the trajectories of the charged particles, a Čerenkov counter (CC) for electron identification, scintillators counters (SC) to measure the time-of-flight (TOF), and an electro-magnetic calorimeter (EC) to identify electrons and neutral particles. The detector covers 80% of the azimuthal angle. The DC and SC subtend polar angles from $8°$ to $142°$, whereas the CC and EC cover up to $45°$.

V. DATA REDUCTION AND ANALYSIS

In this article we report the measurement of target and double spin asymmetries for the $\vec{p}(\vec{e}, e'p)\pi^0$ channel using the 1.6-GeV beam on $^{15}NH_3$ target data set.

A. Channel identification

The exclusive final state $\vec{p}(\vec{e}, e'p)\pi^0$ was selected by identifying an electron, a proton, and a missing pion. Electrons are identified at the trigger level by requiring a coincidence signal from the CC and the EC, and the offline track reconstruction reduces the electron candidates by geometrically matching signals from the DC, CC, and EC. Electron identification was further improved in the data analysis to reduce contamination from negative particles such as π^- and other sources of background. The z-vertex position was used to remove events originating from scattering off the target windows. To improve the resolution of the vertex position, the data were corrected to account for the effect on the vertex reconstruction due to the beam rastering. Figure 3 shows the vertex position before and after the correction, and the applied cut, -58 cm $< z$ vertex < -52 cm, to select events originating inside the $^{15}NH_3$ target.

To separate electrons from negative pions, a combinations of cuts on the Čerenkov and the EC signals were imposed. The energy released by electrons traversing the EC is proportional to their momentum, and about 30% of this energy deposition
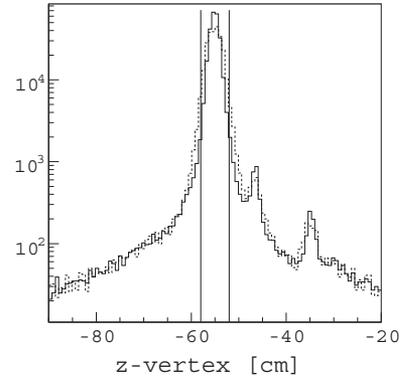

FIG. 3. Number of electron events as a function of the vertex z position. The dashed and the solid lines represent the distribution before and after the raster correction, respectively. The vertical lines indicate the cut applied to the data to remove the peaks coming from the scattering off the exit windows of the target.

is measured by the scintillator sheets in the EC (sampling fraction). To reject negative pions, a cut on the total EC visible energy as a function of the momentum was applied. The energy deposited in the EC is also measured separately for the inner part and the outer part. A cut to reject events with a low-energy deposition in the inner part of the calorimeter was applied. This allows further identification of electrons, which shower mostly in the inner part of the EC, whereas pions are minimum ionizing and lose most of their energy in the outer part.

In CLAS, positive hadrons are identified using the momentum and the path length information from the DC and the timing information from the SC. Figure 4 shows the cut applied to select protons, which appear well separated from positive pions at the energy of this experiment. The missing pions were selected by a 2σ cut on the missing mass $M_X^2 = |p_e + p_p - p_{e'} - p_{p'}|^2$ spectrum around the mass of the pion. In addition, to reduce multipion background, events with detected charged particles other than the electron and the proton in the final state were rejected.

B. Fiducial cuts and acceptance corrections

The objective of this analysis is to extract asymmetries, for which the precise knowledge of the acceptance is not
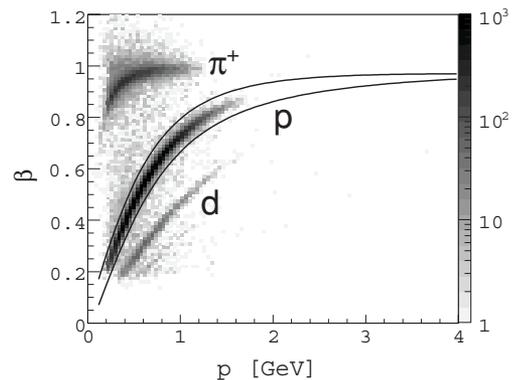

FIG. 4. β vs. p for positively charged particles. The lines show how protons are selected in the analysis.

as crucial as for differential cross-section measurements. Nevertheless, the acceptance can still affect the results. To calculate asymmetries, the ratio of counts integrated over ranges of ϕ^*, θ^*, Q^2, and W is formed, and because the acceptance depends on these variables, it does not necessarily cancel. Fiducial cuts were applied to the data in order to remove regions where the efficiency varies by more than one order of magnitude, and the acceptance was calculated analytically for the geometrical regions defined by the fiducial cuts. This procedure fully corrects the data for the acceptance except for an overall efficiency factor that is assumed to be constant within the fiducial cuts and that will therefore cancel out when taking the ratios in the asymmetries.

C. Experimental definition of the asymmetries

For each helicity configuration, the number of events can be written as:

$$
N_{\uparrow\uparrow} = D_1\left(\sigma_0 + \sigma_0^N + P_e^a\sigma_e + P_e^a\sigma_e^N + P_t^a\sigma_t + P_e^a P_t^a\sigma_{\text{et}}\right)
$$
$$
N_{\downarrow\uparrow} = D_2\left(\sigma_0 + \sigma_0^N - P_e^a\sigma_e - P_e^a\sigma_e^N + P_t^a\sigma_t - P_e^a P_t^a\sigma_{\text{et}}\right)
$$
$$
N_{\uparrow\downarrow} = D_3\left(\sigma_0 + \sigma_0^N + P_e^b\sigma_e + P_e^b\sigma_e^N - P_t^b\sigma_t - P_e^b P_t^b\sigma_{\text{et}}\right)
$$
$$
N_{\downarrow\downarrow} = D_4\left(\sigma_0 + \sigma_0^N - P_e^b\sigma_e - P_e^b\sigma_e^N - P_t^b\sigma_t + P_e^b P_t^b\sigma_{\text{et}}\right),
$$
$$
\tag{14}
$$

where the arrows in $N_{\uparrow\uparrow}$, $N_{\uparrow\downarrow}$, $N_{\downarrow\uparrow}$, and $N_{\downarrow\downarrow}$ indicate the beam and the target polarizations, respectively. Because the target was the same for all configurations, the parameters D_1 through D_4 differ only by the total accumulated charge Q. P_e^a and P_t^a are the beam and target polarizations for runs with a positively polarized target and P_e^b and P_t^b for negative target polarization runs. The beam polarizations for the groups $(N_{\uparrow\uparrow}, N_{\downarrow\uparrow})$ and $(N_{\uparrow\downarrow}, N_{\downarrow\downarrow})$ are assumed to be equal because the polarization of the beam was reversed every half second, and therefore each pair was taken at the same time. However, the target polarization was changed on a time scale of several days, and therefore the corresponding beam polarization could be different during these different periods. The terms $\sigma_0, \sigma_e, \sigma_t$, and σ_{et} represent the cross sections for scattering of polarized electrons off a longitudinally polarized proton in the ^{15}NH$_3$ target, whereas the terms σ_0^N and σ_e^N were added to take into account that there are additional contributions coming from the seven unpolarized protons bound in the nitrogen nucleus. The asymmetries may be written in terms of these quantities as:

$$
A_t = \frac{\sigma_t}{\sigma_0} = \frac{1}{P_t^b} \frac{(\overline{N_{\uparrow\uparrow}} + \overline{N_{\downarrow\uparrow}}) - (\overline{N_{\uparrow\downarrow}} + \overline{N_{\downarrow\downarrow}})}{(\overline{N_{\uparrow\uparrow}} + \overline{N_{\downarrow\uparrow}}) + \alpha_t(\overline{N_{\uparrow\downarrow}} + \overline{N_{\downarrow\downarrow}}) - CN^{\text{BG}}},
$$
$$
\tag{15}
$$

$$
A_{\text{et}} = -\frac{\sigma_{\text{et}}}{\sigma_0}
$$
$$
= \frac{1}{P_e^a P_t^b} \frac{-(\overline{N_{\uparrow\uparrow}} - \overline{N_{\downarrow\uparrow}}) + \alpha_e(\overline{N_{\uparrow\downarrow}} - \overline{N_{\downarrow\downarrow}})}{(\overline{N_{\uparrow\uparrow}} + \overline{N_{\downarrow\uparrow}}) + \alpha_t(\overline{N_{\uparrow\downarrow}} + \overline{N_{\downarrow\downarrow}}) - CN^{\text{BG}}},
$$
$$
\tag{16}
$$

where the counts were normalized to the same total charge. In these expressions,

$$
\overline{N_{\uparrow\uparrow}} \equiv \frac{D_2}{D_1}N_{\uparrow\uparrow} \quad \overline{N_{\downarrow\uparrow}} \equiv N_{\downarrow\uparrow}
$$
$$
\tag{17}
$$
$$
\overline{N_{\uparrow\downarrow}} \equiv \frac{D_2}{D_1}N_{\uparrow\downarrow} \quad \overline{N_{\downarrow\downarrow}} \equiv \frac{D_2}{D_4}N_{\downarrow\downarrow}
$$

and

$$
\alpha_e = \frac{P_e^a}{P_e^b} \quad \alpha_t = \frac{P_t^a}{P_t^b}.
$$
$$
\tag{18}
$$

The term CN^{BG} represents the properly normalized ^{12}C and ^{4}He counts used to simulate and remove the residual background contribution $2D_2(1 + \alpha_t)\sigma_0^N$ in the denominator. The experimental determination of the normalization constant C is discussed in the next section.

D. Nuclear background subtraction

The data contain a large background coming from scattering off ^{15}N and the ^{4}He from the target cooling bath. Data on ^{12}C and ^{4}He targets were used to remove these contributions. The procedure to determine the term CN^{BG} consists of two steps. The first step was to determine how to combine the ^{12}C and ^{4}He data to correct for the different amount of ^{4}He displaced by the ^{15}NH$_3$ and ^{12}C targets. Using a calculation based on target thicknesses, densities, and window contributions, the background counts were constructed as $N^{\text{BG}} = N^{12}\text{C} - 0.22N^4\text{He}$. The second step consists of the determination of the normalization constant C. The normalization constant is W dependent because of the different ratio of protons to neutrons for the ^{15}N and ^{12}C targets. The constant C was extracted by normalizing the missing mass spectra of the ^{15}N and the constructed background to each other in the negative missing mass region, where one has only events stemming from scattering off background nuclei. Because the missing mass spectra show a dependence on the center-of-mass polar angle of the proton, θ^*, the normalization constant was extracted for each W and $\cos\theta^*$ bin. Figure 5 shows a sample of missing mass spectra for the ^{15}NH$_3$, the background, and
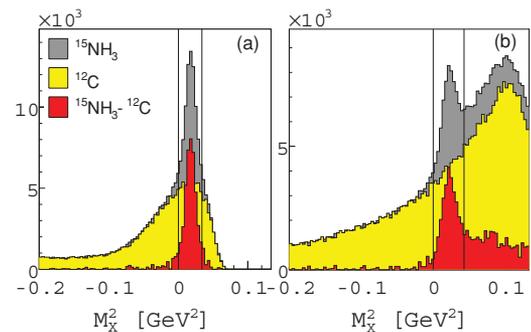
FIG. 5. (Color online) M_x^2 spectra of ^{15}NH$_3$, normalized ^{12}C, and their subtraction for $0 < \cos\theta < 0.2$ and invariant masses of 1.15 GeV $< W <$ 1.2 GeV (a) and 1.4 GeV $< W <$ 1.5 GeV (b). The lines show the 2σ cut applied to select π^0 events.

the subtraction. The figure also shows the cut applied to select neutral pions.

E. Multipion background correction at high W

At higher invariant mass, W, background from the lower missing mass tail of multipion events contaminates the π^0 signal, as can be seen in the right panel of Fig. 5. The measured asymmetry, A_{exp}, found by combining the number of counts [see Eqs. (15) and (16)] is therefore given by

$$A_{\mathrm{exp}} = f_{\pi^0} A_{\pi^0} + f_{\mathrm{back}} A_{\mathrm{back}}, \qquad (19)$$

where A_{π^0} and A_{back} are the asymmetries of π^0 and background events, respectively, f_{π^0} is the ratio of π^0 events to total events, and $f_{\mathrm{back}} = 1 - f_{\pi^0}$ is the fraction of background events. Equation (19) was used to extract A_{π^0}. A_{back} was measured using the same analysis procedure used for A_{exp}, except that events were selected with a missing mass squared greater than the pion mass squared and less than 0.2 GeV^2. The values of the background asymmetry A_{back} vary from 1% to 30% depending on the kinematic bin. The fraction f_{back} was found by fitting the missing mass spectrum, consisting of the pion peak and the background, with two Gaussian curves and using those to estimate the number of background and pions events in the region selected by the cut. The fraction was found to be increasing with the invariant mass as expected from a value of 1.2% for 1.25 GeV $< W <$ 1.3 GeV up to 12% for 1.6 GeV $< W <$ 1.7 GeV. The overall correction $f_{\mathrm{back}} A_{\mathrm{back}}$ was from 0.5 to 2.5%.

F. $P_e P_t$ determination

The product of the beam and target polarizations, $P_e P_t$, was determined by comparing the measured elastic asymmetry A_{meas} with the predicted value A_{theo},

$$P_e P_t = \frac{A_{\mathrm{theo}}}{A_{\mathrm{meas}}}, \qquad (20)$$

where

$$A_{\mathrm{meas}} = \frac{N_{\uparrow\uparrow} - N_{\downarrow\uparrow}}{N_{\uparrow\uparrow} + N_{\downarrow\uparrow}} = \frac{P_e P_t \sigma_{\mathrm{et}}}{\sigma_0} \qquad (21)$$

and [34]

$$A_{\mathrm{theo}}$$
$$= -\frac{\cos\theta_\gamma \sqrt{1-\epsilon^2} + \left(\frac{Q^2}{4M^2}\right)^{-\frac{1}{2}} \sqrt{2\epsilon(1-\epsilon)} \sin\theta_\gamma \cos\phi_\gamma \frac{G_E}{G_M}}{\epsilon\left(\frac{Q^2}{4M^2}\right)^{-1}\left(\frac{G_E}{G_M}\right)^2 + 1}. \qquad (22)$$

For the Q^2 range in this analysis, $\frac{G_E}{G_M} \sim \mu_p$, where μ_p is the magnetic moment of the proton ($\mu_p = \frac{1}{2}g$ where $g = 5.5856912$). The product of beam and target polarization ($P_e P_t$) was independently determined in six Q^2 bins and then the average value of these six results was calculated. Figure 6 shows the results for the positive ($P_e P_t^a$) and negative target polarization data ($P_e P_t^b$). These measurements allow one to extract target polarizations P_t^a, P_t^b by simply taking the ratio of these products and the measured beam polarization P_e.
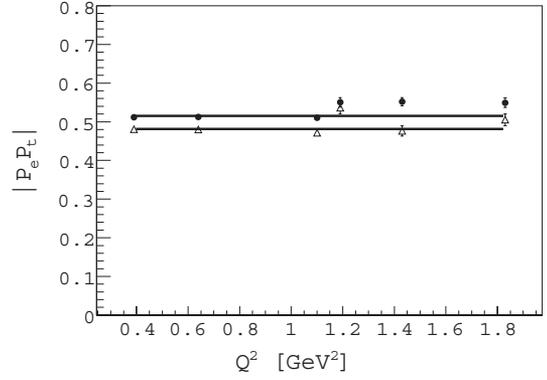

FIG. 6. The product $|P_e P_t|$ as a function of Q^2 for positive (filled circles) and negative (open triangles) target polarization runs. The six values for each polarization were fitted with a constant to obtain the average values $P_e P_t^a = 0.517 \pm 0.002$ and $P_e P_t^b = -0.483 \pm 0.003$.

G. Bin centering corrections

To reduce effects due to the width of the kinematic bins in Q^2, W, $\cos\theta^*$, and ϕ^*, a bin centering correction was applied to the data. This correction is model dependent and to minimize the error, the models that describe the data best were chosen. The Sato and Lee [4,35] and MAID07 [3] models were used for the $\Delta(1232)$ and the higher W region, respectively. Neither model includes the data presented in this article in their fits. The bin centering correction is defined as:

$$\beta = \frac{\sigma_{\mathrm{exact}}}{\sigma}, \qquad (23)$$

where σ_{exact} is the model cross section obtained at the center values of our bins, and σ is the model cross section averaged over the bins in the analysis. This correction was calculated for each beam and target polarization configuration and applied individually to the number of counts $\overline{N_{\uparrow\uparrow}}$, $\overline{N_{\downarrow\uparrow}}$, $\overline{N_{\uparrow\downarrow}}$, and $\overline{N_{\downarrow\downarrow}}$ before constructing the asymmetries as described in Eqs. (15) and (16).

H. Systematic uncertainties

Several sources of systematic uncertainties were identified in the analysis procedure. For most cases, the technique used to estimate the size of these uncertainties was to vary individual parameters in the analysis, recalculate the asymmetries, and compare the new results to the original values.

One of the main sources of uncertainties is due to the correction for nitrogen, which was estimated using a ^{12}C target. The statistical uncertainty on the normalization procedure is very small; however, the whole procedure is based on the assumption that the ^{12}C target spectrum has a similar shape as the ^{15}NH$_3$ background. Based on studies in the elastic region, the normalization factor was found to be known with a precision of 3–4%. The asymmetry was recalculated using a normalization factor changed by 3.5%, and the comparison shows a point by point variation of the asymmetry on the order of 4–8%.

A second source of systematic uncertainties is due to the uncertainties of the beam and target polarization values. The

beam polarization is measured with the Møller polarimeter and it is know with an accuracy of 2%, which results in a systematic uncertainty on the asymmetry up to 2%. The target polarization, extracted from the product $P_e P_t$ as described in Sec. V F, has a systematic and statistical uncertainty associated with it. The statistical uncertainty gives a negligible systematic variation of the asymmetry, whereas the systematic error due to the uncertainty of the ratio G_E/G_M and to the carbon normalization gives a total systematic uncertainty on the asymmetry of 3.2%.

Another source of error is the model dependence of the bin centering correction. To study this effect a different model, MAID03, was used for the correction and the difference was assigned as a systematic uncertainty. A point by point variation from 1 to 15% was found depending on the W range and the asymmetry considered. For the most part these uncertainties were negligible compared to the statistical error.

The multipion background correction requires an estimate of the number of events contaminating the pion sample, f_{back}. The fraction has both a statistical and systematic uncertainty that contributes to the systematic uncertainty of the asymmetry. The main source of systematic uncertainty was the assumption that the background does not depend on the polar angle of the pion in the center-of-mass, θ^*. An overall uncertainty of 20% was assigned to f_{back}, to account for fluctuations in different $\cos\theta^*$ intervals. A change of this amount causes a point-by-point variation in the asymmetry up to 10%, most of the time negligible compared to the statistical uncertainty.

The effect of cuts was studied as well, in particular the fiducial and missing mass cuts. To study the impact of these cuts on the analysis, the asymmetries were measured using complementary cuts and compared to each other. The two sets of data points were found statistically compatible and therefore no systematic uncertainty was assigned.

The overall systematic uncertainties were found by combining the different contributions in quadrature and are reported point by point in the CLAS Physics Data Base [36]. It was found that the systematic uncertainties were smaller than the statistical ones for most of the data points.

VI. RESULTS

Target (A_t) and double spin (A_{et}) asymmetries were measured as a function of the invariant mass W, the momentum transfer squared Q^2, and the center-of-mass pion angles, θ^* and ϕ^*. The data were divided into 8 bins in W, 3 bins in Q^2, 10 bins in $\cos\theta^*$, and 15 bins in ϕ^*. The results consist of 2435 data points for each asymmetry, after eliminating bins with nearly zero acceptance. Table I summarizes the binning and Fig. 7 illustrates the kinematic coverage in Q^2 and W.

The results were compared with five theoretical approaches: MAID07, MAID03, MAID00, and the DMT model everywhere, and the Sato and Lee model in the $\Delta(1232)$ region. Figures 8 and 9 show a sample of the results as a function of $\cos\theta^*$. The error bars indicate the statistical uncertainties, whereas the brown boxes indicate the systematic uncertainties. The complete numerical results are reported in the CLAS

TABLE I. Binning for the $1.6 - \mathrm{GeV}$ data set.

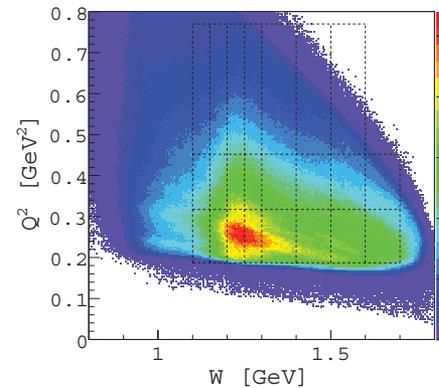| Bin	Range	Bin size	No. of bins
	1.1–1.3 GeV	0.05 GeV	4
W	1.3–1.7 GeV	0.10 GeV	4
	0.187–0.317 GeV^2	0.130 GeV^2	1
Q^2	0.317–0.452 GeV^2	0.135 GeV^2	1
	0.452–0.770 GeV^2	0.318 GeV^2	1
$\cos\theta^*$	-1.0–1.0	0.2	10
ϕ^*	$-180°$–$180°$	$24°$	15

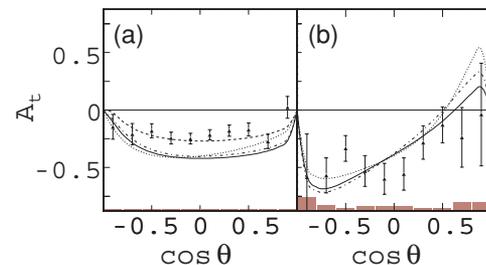FIG. 7. (Color online) Kinematic coverage in Q^2 and W. The dashed lines indicate how the data were subdivided.

FIG. 8. (Color online) The target asymmetries A_t for $Q^2 = 0.385$ GeV^2, $\phi^* = 120°$, and invariant masses $W = 1.225$ GeV (a) and $W = 1.35$ GeV^2 (b). Systematic uncertainties are shown as shaded bars. The curves correspond to the MAID07 (solid), DMT (dotted), Sato and Lee (dashed), and MAID03 (dashed dotted) calculations.
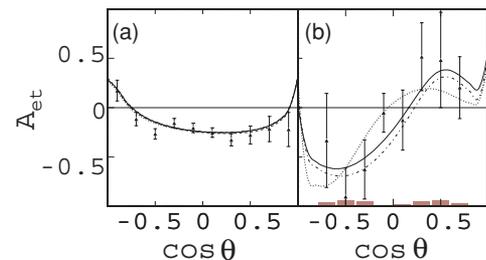

FIG. 9. (Color online) The target asymmetries A_{et} for $Q^2 = 0.252$ GeV^2, $\phi^* = 120°$, and invariant masses $W = 1.225$ GeV (a) and $W = 1.65$ GeV (b). Systematic uncertainties are shown as shaded bars. The curves correspond to the MAID07 (solid), DMT (dotted), Sato and Lee (dashed), and MAID03 (dashed dotted) calculations.
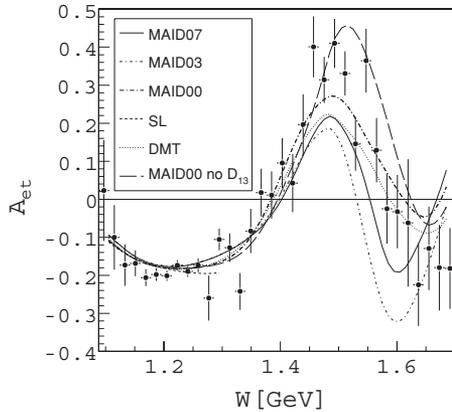
FIG. 10. A_{et} as a function of the invariant mass W, integrated over the whole range in $\cos\theta^*$, Q^2, and $60° < \phi^* < 156°$. The curves correspond to the MAID07 (solid), DMT (dotted), Sato and Lee (dashed), MAID03 (dashed dotted), MAID00 (long-dashed-dotted) calculations. The long-dashed curve is the MAID00 calculation without the $D_{13}(1520)$ contribution.

Physics Data Base [36]. We see that the models reproduce well the general trends of the data. The asymmetry signs and the sign changes are generally predicted correctly. Discrepancies are visible at the quantitative level and are different for different models as discussed in Sec. VI A. This shows the sensitivity of this data set to the specific model ingredients for the resonant and nonresonant amplitudes in the first, second, and third resonance regions.

Integrated asymmetries were also extracted as a function of the invariant mass W and the momentum transfer Q^2. The asymmetries as a function of the invariant mass were calculated integrating over the whole range in $\cos\theta^*$, Q^2, and over a partial range in ϕ^* from 60° to 156° to avoid regions with acceptance less than 2%. Figures 10 and 11 show the results compared to the models. The asymmetries as a function of the momentum transfer were calculated integrating over the
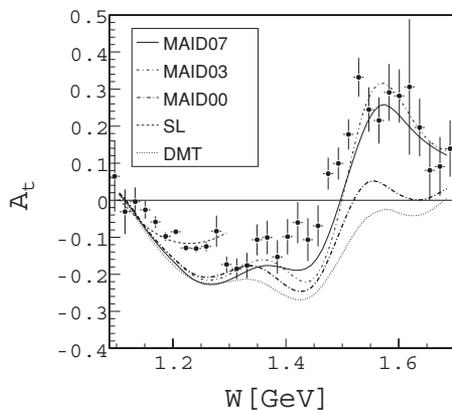

FIG. 11. A_t as a function of the invariant mass W, integrated over the whole range in $\cos\theta^*$, Q^2, and $60° < \phi^* < 156°$. The curves correspond to the MAID07 (solid), DMT (dotted), Sato and Lee (dashed), MAID03 (dashed dotted), and MAID00 (long-dashed-dotted) calculations.

whole range in $\cos\theta^*$, over a partial range in ϕ^* from 60° to 156°, and over 12 bins in W from 1.1 to 1.7 GeV in steps of 0.05 GeV. Figures 12 and 13 show the results compared to the models.

Figure 12 shows the Q^2 dependence of the double spin asymmetry A_{et} for 12 bins in W. The negative asymmetry and the approximate linear dependence on Q^2, as well as the negative slope observed in the region of the $\Delta(1232)$ resonance, are well described by all models. In the mass region of the Roper resonance $P_{11}(1440)$, and the $D_{13}(1520)$ and $S_{11}(1535)$ resonances at $1.45 < W < 1.60$ GeV, the asymmetry is large, positive, and increases rapidly with Q^2. The DMT and MAID models all underestimate the magnitude. The strength of the $P_{11}(1440)$ in this low Q^2 range is known to be small [6], and the $S_{11}(1535)$ has been well measured in η electroproduction. The excitation strength of the $D_{13}(1520)$ and the relative strength of the $A_{1/2}$ and $A_{3/2}$ amplitudes of this resonance are the main source of uncertainty. The discrepancy with model parametrizations is likely related to an overestimation of the relative strength of the dominant $A_{3/2}$ amplitude in comparison with the $A_{1/2}$. This sensitivity to the dominant $A_{3/2}$ amplitudes is also shown in Fig. 10, where the magnitude of the computed A_{et} increases without the $D_{13}(1520)$ resonance contribution, bringing it in better agreement with the data in the mass range near 1520 MeV. In the mass range $1.6 < W < 1.7$ GeV the $F_{15}(1680)$ is the dominant resonance. The asymmetry increases rapidly with Q^2 and changes sign at $Q^2 \sim 0.35$ GeV^2. The MAID07 model approximately describes the Q^2 dependence, including the sign change. We remark that the observed behavior of A_{et} with Q^2 in the region above the $\Delta(1232)$ is consistent with the behavior measured in the $n\pi^+$ channel [30].

The target asymmetry A_t depends on the imaginary part of interferences involving resonant and nonresonant amplitudes, and its interpretation is less straightforward than the double spin asymmetry. The asymmetry A_t is shown in Fig. 13 as a function of Q^2. There is not a simple explanation of the discrepancies between the models and data for this observable, as the results may depend on the phases of amplitudes that are also strongly energy-dependent. In contrast to the double spin asymmetry, A_t is well described in the mass region of the $\Delta(1232)$ only by the SL model, while the DMT and MAID parametrizations show significant discrepancies with the data. The higher-mass regions are reasonably well described by the MAID parametrizations, whereas the DMT model shows strong discrepancies, including the wrong sign for the four higher-mass bins.

A. χ^2 comparison

To evaluate in a more rigorous way how well the models describe the data, a χ^2 comparison was performed. The χ^2 was defined as:

$$\chi^2 = \sum_i \frac{\left(x_i^{\text{data}} - x_i^{\text{model}}\right)^2}{\left(\sigma_i^{\text{data}}\right)^2}, \qquad (24)$$

where x_i^{data} is the value of each experimental point for all the asymmetries and x_i^{model} is the corresponding value of the

TABLE II. χ^2 per number of degree of freedom (ndf) comparison between the data and the five models.

Model	A_t	A_{et}	A_t	A_{et}
	$W < 1.3$ GeV ndf = 1306		$W > 1.3$ GeV ndf = 1129	
MAID07	1.98	1.04	0.99	1.30
MAID03	1.75	1.05	1.20	1.86
MAID00	1.97	1.03	1.97	1.07
SL	1.00	1.05	–	–
DMT	2.09	1.02	1.71	1.17

theoretical prediction. Because the model is given without errors, only the experimental statistical uncertainties σ_i^{data} were used in the denominator. The comparison gave the results listed in Table II. The calculation led us to make a few conclusions about the models. First, in the $\Delta(1232)$ region, all the models are in good agreement with the measured double spin asymmetry, A_{et}. This is not surprising because A_{et} is dominated by the resonance multipoles (i.e., $|M_{1+}|^2$, $\text{Re}\{E_{1+}^* M_{1+}\}$) [31] that dominate the unpolarized cross section. Because the model fits are based on unpolarized cross sections, this agreement is expected. At higher W none of the models give a consistently good description of the data for both the target and the double spin asymmetry. The MAID07 parametrization shows improvements for A_t over previous versions, whereas A_{et} is not as well reproduced as by the older MAID00 version. At this level it is not possible to draw further conclusions and only including these data in a new global fit for these models will give a better understanding of the sensitivity of the data and possibly identify the origin of the discrepancies.

VII. SUMMARY

In this article we have presented a set of longitudinal target polarization asymmetries A_t and beam-target double polarization asymmetries A_{et} for the reaction $ep \rightarrow ep\pi^0$ covering the first, second, and part of the third nucleon resonance regions in a wide range of azimuthal and polar center-of-mass angles for the final state π^0. The data also cover a range in photon virtuality Q^2. For the first time, target polarization asymmetries have been measured in the resonance region and in the mass range above the $\Delta(1232)$ resonance. The new data complement the already published results obtained in the $\Delta(1232)$ region [13] for different kinematics. Longitudinal target asymmetries and beam-target asymmetries were measured in 2435 bins each. The polarization asymmetries show strong sensitivity to both resonant and nonresonant amplitudes and are highly selective of model parametrizations for amplitudes underlying the π^0 electroproduction process. Due to the large number of data points, only samples of specific kinematics and integrated quantities are compared with model predictions. Although the models agree well with the double spin asymmetries in the $\Delta(1232)$ mass region, three of the four models surveyed have a substantial disagreement beyond the $\Delta(1232)$ region and all models show a significant disagreement with the single spin target asymmetry data. The discrepancies, when quantified using the statistical interpretation from Ref. [37] of the χ^2 values in Table II above, amount to less than a 5% probability that the measured double spin asymmetry data set A_{et} would be consistent with any of the given models for W above the $\Delta(1232)$. For the single spin target asymmetry A_t the probability is less than 59%. The full impact of the complete data set on our understanding of the nucleon structure in the regime of strong QCD and confinement can be obtained only by including these new data sets in global analyses that incorporate all exclusive pion electroproduction cross sections and polarization observables. This effort is currently underway
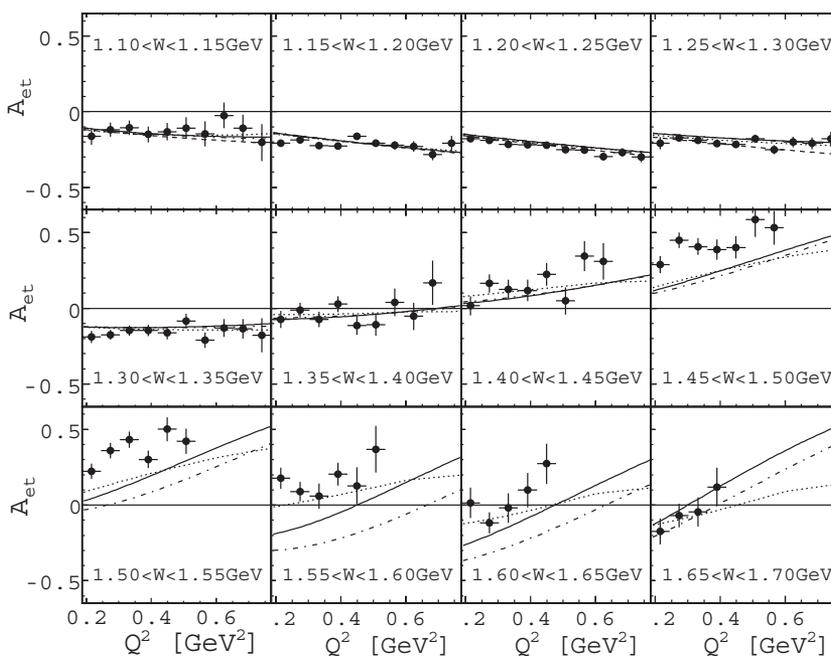

FIG. 12. A_{et} as a function of the photon virtuality Q^2, integrated over the whole range in $\cos\theta^*$, $60° < \phi^* < 156°$, and 12 invariant mass regions from 1.1 to 1.7 GeV in steps of 0.05 GeV. The curves correspond to the MAID07 (solid), DMT (dotted), Sato and Lee (dashed), and MAID03 (dashed dotted) calculations.
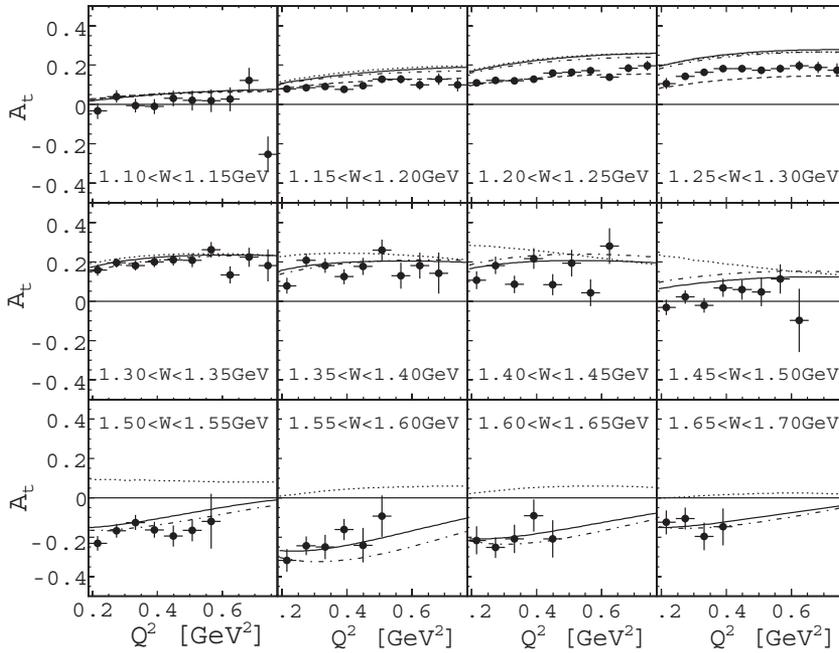
FIG. 13. A_t as a function of the photon virtuality Q^2, integrated over the whole range in $\cos\theta^*$, $60° < \phi^* < 156°$, and 12 invariant mass regions from 1.1 to 1.7 GeV in steps of 0.05 GeV. The curves correspond to the MAID07 (solid), DMT (dotted), Sato and Lee (dashed), and MAID03 (dashed dotted) calculations.

and is the subject of forthcoming publications [38]. The full set of data is available at the CLAS Physics Data Base [36].

[1] Nathan Isgur, in Newport News 2000, Excited Nucleons and Hadronic Structure, 403–422, edited by V. D. Burkert, L. Eloaudrhiri, J. J. Kelley, and R. C. Minehart, http://www.slac.stanford.edu/spires/find/hep/www?irn=4417968.

[2] S. S. Kamalov, G. Y. Chen, S. N. Yang, D. Drechsel, and L. Tiator, Phys. Lett. **B522**, 27 (2001).

[3] D. Drechsel, S. S. Kamalov, and L. Tiator, Eur. Phys. J. A **34**, 69 (2007).

[4] T. Sato and T. S. H. Lee, Phys. Rev. C **63**, 055201 (2001).

[5] I. G. Aznauryan, Phys. Rev. C **67**, 015209 (2003).

[6] I. G. Aznauryan, V. D. Burkert, H. Egiyan, K. Joo, R. Minehart, and L. C. Smith, Phys. Rev. C **71**, 015201 (2005).

[7] V. D. Burkert and T. S. H. Lee, Int. J. Mod. Phys. E **13**, 1035 (2004).

[8] V. Frolov *et al.*, Phys. Rev. Lett. **82**, 45 (1999).

[9] K. Joo *et al.*, Phys. Rev. Lett. **88**, 122001 (2002).

[10] K. Joo *et al.*, Phys. Rev. C **68**, 032201 (2003).

[11] K. Joo *et al.*, Phys. Rev. C **70**, 042201 (2004).

[12] N. F. Sparveris *et al.*, Phys. Rev. C **67**, 058201 (2003).

[13] A. Biselli *et al.*, Phys. Rev. C **68**, 035202 (2003).

[14] J. J. Kelly *et al.*, Phys. Rev. Lett. **95**, 102001 (2005).

[15] M. Ungaro *et al.*, Phys. Rev. Lett. **97**, 112003 (2006).

[16] S. Stave *et al.*, Eur. Phys. J. A **30**, 471 (2006).

[17] C. Alexandrou, P. deForcrand, H. Neff, J. W. Negele, W. Schroers, and A. Tsapalis, Phys. Rev. Lett. **94**, 021601 (2005).

[18] C. Alexandrou *et al.*, Phys. Rev. D **69**, 114506 (2004).

[19] H. Egiyan *et al.*, Phys. Rev. C **73**, 025204 (2006).

[20] K. Park *et al.*, Phys. Rev. C **77**, 015208 (2008).

[21] C. S. Armstrong *et al.*, Phys. Rev. D **60**, 052004 (1999).

[22] R. Thompson *et al.*, Phys. Rev. Lett. **86**, 1702 (2001).

[23] H. Denizli *et al.*, Phys. Rev. C **76**, 015204 (2007).

[24] M. Ripani *et al.*, Phys. Rev. Lett. **91**, 022002 (2003).

[25] S. Strauch *et al.*, Phys. Rev. Lett. **95**, 162003 (2005)

[26] K. Joo *et al.*, Phys. Rev. C **72**, 058202 (2005).

[27] R. Fatemi *et al.*, Phys. Rev. Lett. **91**, 222002 (2003).

[28] J. Yun *et al.*, Phys. Rev. C **67**, 055204 (2003).

[29] P. Bosted *et al.*, Phys. Rev. C **75**, 035203 (2007).

[30] R. De Vita *et al.*, Phys. Rev. Lett. **88**, 082001 (2002).

[31] D. Drechsel and L. Tiator, J. Phys. G **18**, 449 (1992).

[32] B. W. Filippone and X. D. Ji, Adv. Nucl. Phys. **26**, 1 (2001).

[33] B. A. Mecking *et al.*, Nucl. Instrum. Methods A **503**, 513 (2003).

[34] T. W. Donnelly and A. S. Raskin, Ann. Phys. **169**, 247 (1986).

[35] T. Sato and T. S. H. Lee, Phys. Rev. C **54**, 2660 (1996).

[36] http://clasweb.jlab.org/physicsdb.

[37] W. M. Yao *et al.* (Particle Data Group), J. Phys. G **33**, 1 (2006).

[38] I. Aznauryan *et al.* (in preparation).